Plasma waves confined to the diamagnetic cavity of comet 67P/Churyumov-Gerasimenko

H. Gunell,[1,2]⋆ C. Goetz,[3] A. Eriksson,[4] H. Nilsson,[5] C. Simon Wedlund,[6]
P. Henri,[7] R. Maggiolo,[1] M. Hamrin,[2] J. De Keyser,[1] M. Rubin,[8]
G. Stenberg Wieser,[5] G. Cessateur,[1] F. Dhooghe,[1] and A. Gibbons[1,9]

[1] *Royal Belgian Institute for Space Aeronomy (BIRA-IASB), Avenue Circulaire 3, 1180 Brussels, Belgium*
[2] *Department of Physics, Umeå University, 901 87 Umeå, Sweden*
[3] *Institut für Geophysik und extraterrestrische Physik, TU Braunschweig, Mendelssohnstr. 3, 38106 Braunschweig, Germany*
[4] *Swedish Institute of Space Physics, Ångström Laboratory, Lägerhyddsvägen 1, Uppsala, Sweden*
[5] *Swedish Institute of Space Physics, Box 812, 981 28 Kiruna, Sweden*
[6] *Department of Physics, University of Oslo, Box 1048 Blindern, 0316 Oslo, Norway*
[7] *LPC2E, CNRS, Orléans, France*
[8] *Physikalisches Institut, University of Bern, Sidlerstrasse 5, 3012 Bern, Switzerland*
[9] *Laboratoire de Chimie Quantique et Photophysique, Université Libre de Bruxelles, 50 Avenue F. D. Roosevelt, B-1050 Brussels, Belgium*

ABSTRACT
Ion acoustic waves were observed in the diamagnetic cavity of comet 67P/Churyumov-Gerasimenko by the Rosetta spacecraft on 3 August 2015, when the comet was 1.25 AU from the Sun. Wave spectra recorded by the Langmuir probe (RPC-LAP) peak near 200 Hz, decrease for higher frequencies, and reach the noise floor at approximately 1.5 kHz. These waves were observed only when the spacecraft was in the diamagnetic cavity or at its boundary, which is identified as a sharp drop in magnetic field magnitude, measured by RPC-MAG. The plasma, on both sides of the boundary, is dominated by a cold (a few hundred K) water group ion population, one cold ($k_B T_e \sim 0.1$ eV) and one warm ($k_B T_e \sim 10$ eV) electron population. The observations are interpreted in terms of current-driven ion acoustic waves, generated by currents that flow through bulges on the boundary of the diamagnetic cavity.

Key words: Comets: individual 67P/Churyumov-Gerasimenko – plasmas – waves – magnetic fields – methods: data analysis – methods: analytic

1 INTRODUCTION

The first observation of the diamagnetic cavity at a comet was made when the Giotto spacecraft flew by comet Halley in 1986 (Neubauer et al. 1986). During two minutes around Giotto's closest approach to the comet's nucleus, the spacecraft passed through a region where the magnetic field was approximately zero. The phenomenon had already been observed at the AMPTE (Active Magnetospheric Particle Tracer Explorer) artificial comet, created by the release of barium in the solar wind (Haerendel et al. 1986). It was shown using analytic models that a diamagnetic cavity can be maintained by a balance between the magnetic pressure of the solar wind and the ion–neutral friction force, stemming from the expanding neutral atmosphere of the comet (Haerendel 1987; Cravens 1987).

The Rosetta spacecraft (Glassmeier et al. 2007a) followed comet 67P/Churyumov-Gerasimenko from August 2014, through its approach of the Sun, reaching perihelion at 1.24 AU in August 2015, and continuing its journey outward again until the mission ended in September 2016. Encounters of the diamagnetic cavity were identified in magnetic field data between April 2015 and February 2016 (Goetz et al. 2016a), the first encounter published from this mission was detected on 26 July 2015 and lasted 25 minutes (Goetz et al. 2016b). The nucleus to spacecraft distance was generally larger than the cavity radius that had been predicted by simulations (e.g. Rubin et al. 2015; Koenders et al. 2015). Observations by Goetz et al. (2016a) and Henri et al. (2017) indicate that the shape of the cavity is not stationary. Instead bulges form on the boundary due to an instability, and the short duration of the periods the spacecraft spent in the cavity corresponds to the duration of such a bulge passing over the spacecraft. The spacecraft velocity in the

⋆ E-mail: herbert.gunell@physics.org

comet frame of reference is typically less than $1\,\mathrm{m\,s^{-1}}$. A dropout of suprathermal electrons at energies of $200\,\mathrm{eV}$ as the spacecraft entered the cavity was found by Nemeth et al. (2016).

The plasma environment of comet 67P/Churyumov-Gerasimenko was surveyed by Odelstad et al. (2015) for the period up to and including March 2015. They reported electron temperatures, T_e, around $5\,\mathrm{eV}$. Eriksson et al. (2017) found that a much colder ($k_\mathrm{B}T_\mathrm{e} \lesssim 0.1\,\mathrm{eV}$) electron population became more abundant later in the mission. The electron population is cooled by collisions with the neutrals, if the neutral density is high enough (Vigren & Galand 2013). Most of the time the Rosetta spacecraft was located outside the region where this cooling process is efficient (Mandt et al. 2016). Ion measurements in the low mass loading regime showed ions following the first part of a cycloid trajectory (Nilsson et al. 2015a), as has been illustrated by simulations (Gunell et al. 2015; Simon Wedlund et al. 2017). Later, at higher mass loading, water group ion trajectories turned more anti-sunward (Nilsson et al. 2015b; Behar et al. 2016a). Simon Wedlund et al. (2016) used measurements of the $\mathrm{He^+}$ to $\mathrm{He^{2+}}$ ratio to estimate the neutral outgassing rate. Hybrid simulations have been used to evaluate the ion measurements at different heliocentric distances during the mission (Behar et al. 2016b; Simon Wedlund et al. 2017). The ion environment throughout Rosetta's accompaniment of comet 67P/Churyumov-Gerasimenko was described by Nilsson et al. (2017). Low frequency waves were found in the magnetic field spectrum shortly after Rosetta arrived at the comet (Richter et al. 2015, 2016). Karlsson et al. (2017) detected signals of lower hybrid waves in the electric field spectrum at $1.5\,\mathrm{AU}$ heliocentric distance. Solar wind interaction with comets in light of the Rosetta mission was further reviewed by Glassmeier (2017).

An ion acoustic wave is a compressional plasma wave at frequencies below the ion plasma frequency. In the long wavelength limit, the frequency of an ion acoustic wave is proportional to its wave number. Ion acoustic waves are heavily damped unless $T_\mathrm{e} \gg T_\mathrm{i}$, the ion temperature. However, even in the heavily damped regime, they may still be driven unstable by the presence of a current (Stringer 1964). The ICE spacecraft detected ion acoustic waves in the bow shock region of comet Giacobini-Zinner (Scarf et al. 1986), and such waves were also found in the foreshock upstream of comet Halley (Oya et al. 1986). Waves were observed in the diamagnetic cavity of the AMPTE artificial comet, and ion acoustic waves were deemed a possible explanation for the low frequency emission bands observed (Gurnett et al. 1985).

At comet 67P/Churyumov-Gerasimenko, Gunell et al. (2017) studied one day of data, obtained by Rosetta on 20 January 2015, and found evidence for ion acoustic waves. Then the comet was at a heliocentric distance of $2.5\,\mathrm{AU}$; the comet–solar wind interaction was dominated by weak mass loading, and no diamagnetic cavity had formed. In this paper, we report observations of ion acoustic waves in the diamagnetic cavity of comet 67P/Churyumov-Gerasimenko in early August 2015, close to perihelion, at a heliocentric distance of $1.25\,\mathrm{AU}$. From the perspective of ion acoustic waves, the most significant difference in plasma properties between the two dates is the presence of a significant cold electron population in the near-perihelion observations reported here.

2 OBSERVATIONS

We use the Langmuir Probe instrument (RPC-LAP) (Eriksson et al. 2007) to observe ion acoustic waves in the diamagnetic cavity, which is identified in magnetic field measurements by the RPC-MAG instrument (Glassmeier et al. 2007b). The interpretation of the wave observations is aided by measurements of ion distributions by the Ion Composition Analyzer of the Rosetta Plasma Consortium (RPC-ICA) (Nilsson et al. 2007), current–voltage characteristics obtained by RPC-LAP, and plasma density measurements by the Mutual Impedance Probe (RPC-MIP) (Trotignon et al. 2007).

2.1 Cavities

The diamagnetic cavity is identified in the magnetometer data as a sharp decrease of the magnetic field, as the spacecraft enters the cavity, followed by a period of low and unchanging magnetic field, which lasts until the spacecraft exits the cavity (Goetz et al. 2016a). The magnetometer has a temperature-dependent offset, which complicates the analysis. However, by assuming the average magnetic field is zero inside the cavity a temperature model of the magnetometer has been constructed and used to correct the rest of the data, which consistently shows near-zero values of the magnetic field in the cavity. While the in-cavity field is not necessarily zero, its magnitude can be confined to $B < 1\,\mathrm{nT}$ for the parts of the diamagnetic cavity that have been visited by Rosetta. Goetz et al. (2016a) identified 665 intervals when Rosetta passed through the diamagnetic cavity. In the following sections, we use their list of cavity identifications as well as their instrument-temperature corrected magnetic field data set. From this list we have picked one day, 3 August 2015, to study in more detail. We first present an overview of that day, and then details from one sample cavity encounter that occurred during the day.

Fig. 1 shows the power spectral density, P_II, of the current to the RPC-LAP probe 1, the three components of the **B** field, the plasma density measured by RPC-MIP, and the differential particle flux of the ions summed over all RPC-ICA viewing directions during twelve hours on 3 August 2015, when the comet was at $1.25\,\mathrm{AU}$ heliocentric distance and the spacecraft at $220\,\mathrm{km}$ cometocentric distance. The periods when the spacecraft passed through the diamagnetic cavity, as identified by Goetz et al. (2016a), are marked by black rectangles in all three panels. The cavity that is marked by a red rectangle is shown in detail in Fig. 2.

2.2 Waves

The power spectral densities shown in Figs. 1 and 2 have been computed from time series data obtained by RPC-LAP, which records the current to the two probes at a sampling frequency of $18750\,\mathrm{Hz}$ in the mode used here. Each time series comprises 1600 samples, and it is thus $85.3\,\mathrm{ms}$ long. These time series are recorded at $160\,\mathrm{s}$ intervals. The white
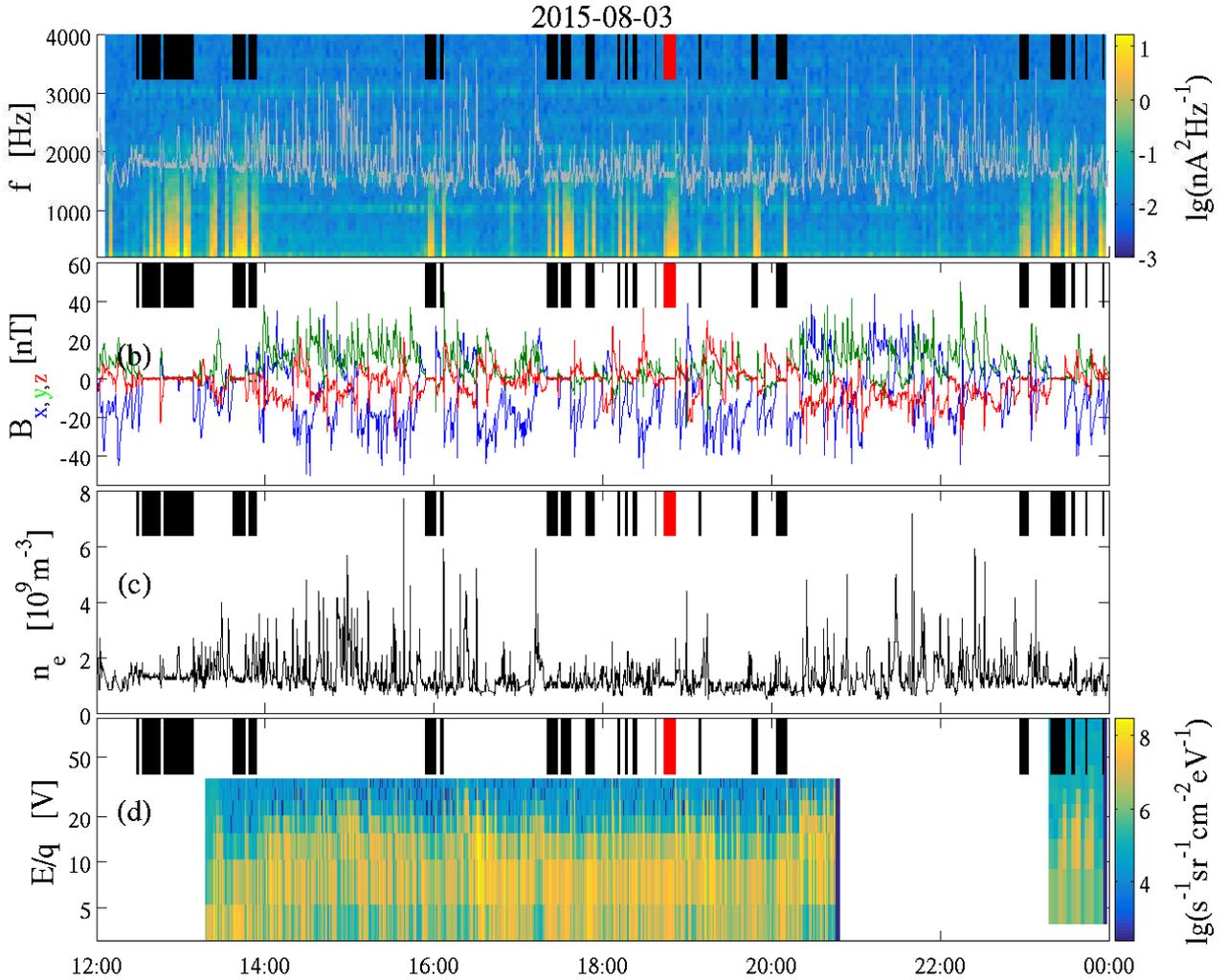
Figure 1. Overview of the observations by the RPC instruments on board the Rosetta spacecraft during the second half of 3 August 2015. **(a)** Power Spectral density of the current to Langmuir probe 1 in the frequency range $200\,\mathrm{Hz} < f \le 4\,\mathrm{kHz}$. The grey curve shows the H_2O^+ ion plasma frequency. **(b)** Components of the magnetic flux density **B** seen by RPC-MAG. **(c)** Plasma density measured by the RPC-MIP instrument. **(d)** Ion energy spectrum measured by RPC-ICA. The colour coded quantity is the differential particle flux summed over all viewing directions. The energy scale has been adjusted for V_{sc} and V_{offset}. The black rectangles shown at the top of each panels mark periods when the spacecraft was inside the diamagnetic cavity, as identified by Goetz et al. (2016a). The red rectangles mark the cavity passage that is shown in more detail in Fig. 2.

spaces between the colour coded spectra in Fig. 2a correspond to the times when no time series were recorded. In Fig. 1 the spectra have been allowed to cover the white spaces to enable viewing of the whole twelve hour period. During the recording of the time series, probe 1 was biased to $+30\,\mathrm{V}$ and probe 2 to $-30\,\mathrm{V}$ with respect to the spacecraft potential. No discernible wave signal could be found on the negatively biased probe 2, and therefore only spectra obtained by probe 1 are shown in the figures. The absence of a wave signal on the negatively biased probe shows that the measured current is dominated by electrons, and the observed signal is therefore proportional to the plasma density variations of the wave.

The spectra in Fig. 2a are also shown as line plots in Fig. 3. The power spectral density recorded when the spacecraft was in the cavity (solid lines) was much higher than

that recorded outside the cavity (dashed lines). The solid black line shows the spectrum recorded at 18:43:12 when the spacecraft was at the boundary of the diamagnetic cavity, and it falls between the two groups in Fig. 3. The plasma density, although highly variable in the magnetised regions, was fairly stable from one cavity encounter to the next. In the cavity it was $n_e \approx 1.0 \times 10^9\,\mathrm{m}^{-3}$, as seen in Fig. 2c. Assuming that all ions are H_2O^+ ions, this means that the ion plasma frequency was $f_{pi} \approx 1.6\,\mathrm{kHz}$.

The wave spectra observed inside the diamagnetic cavity show a broad peak near $200\,\mathrm{Hz}$ and fall off slowly at higher frequencies, reaching the noise floor near the ion plasma frequency. In Fig. 3, the peaks that are seen at 1.0, 1.5, and $2.0\,\mathrm{kHz}$ are artefacts generated by the spacecraft. These are also seen as horizontal stripes in Fig. 1a. The lowest frequency bins are liable to pick up low frequency noise,
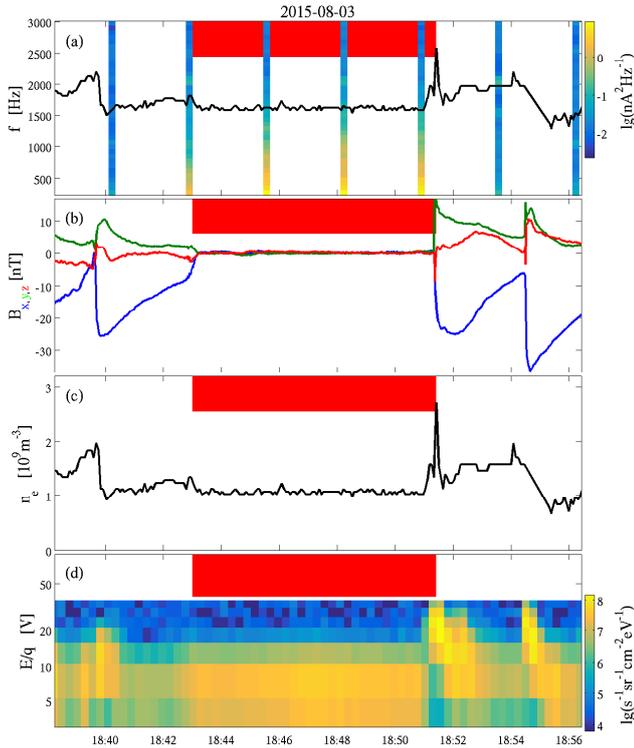
Figure 2. Details of the data from a single passage through the diamagnetic cavity. **(a)** Power Spectral density of the current to Langmuir probe 1 in the frequency range $200\,\mathrm{Hz} < f \leq 3\,\mathrm{kHz}$. The black curve shows the H_2O^+ ion plasma frequency. **(b)** The three components of the magnetic flux density **B** seen by RPC-MAG. **(c)** Plasma density measured by the RPC-MIP instrument. **(d)** Ion energy spectrum measured by RPC-ICA. The colour coded quantity is the differential particle flux summed over all viewing directions. The energy scale has been adjusted for V_{sc} and V_{offset}. The red rectangles mark the duration of the cavity, as it was identified by Goetz et al. (2016a).

and therefore the colour coded spectra in Figs. 1a and 2a are shown only for frequencies above 200 Hz.

Fig. 2 shows that the waves appear only in the diamagnetic cavity or at the boundary. In Fig. 1 waves are seen during the spacecraft traversals of the cavity. During the twelve hour span of the figure, there are a few cases, for example at 12:08 and 13:20, of wave signals registered during periods that were not identified as cavity passages. To examine these cases in more detail, we investigate the relationship between wave activity and the spacecraft position relative to the boundary of the diamagnetic cavity. We integrate the power spectral density in the range $200\,\mathrm{Hz} < f < 1500\,\mathrm{Hz}$ obtaining the power

$$\int_{200\,\mathrm{Hz}}^{1500\,\mathrm{Hz}} P_{II}(f)\,df$$

for each time series. The integral is normalised to the highest value during the day, and this is shown in Fig. 4 together with the magnitude of the magnetic flux density *B* normalised in the same way. In the figure, the cavities are marked by light blue areas.

There are two reasons why high wave power values are
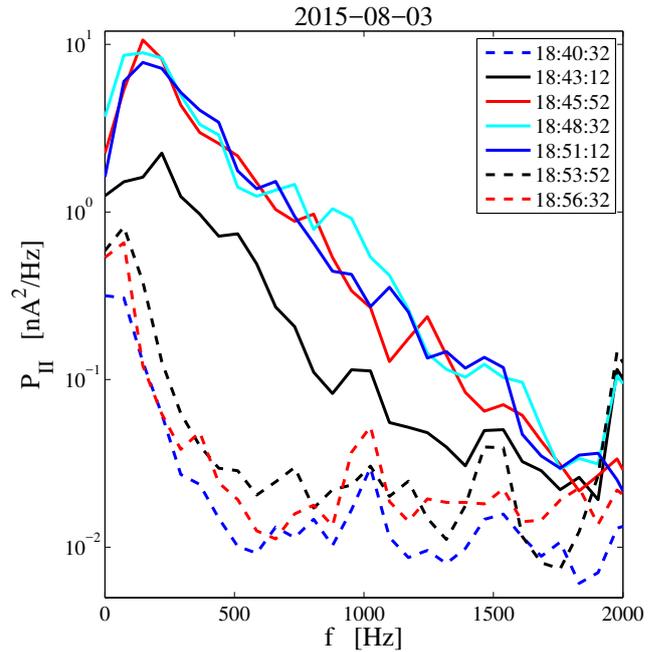

Figure 3. Line plots of the spectra for the cavity encounter shown in Fig. 2a. The dashed lines show spectra obtained outside the cavity. The black solid line shows the spectrum recorded at 18:43:12 when the spacecraft was at the boundary, about to enter the cavity.
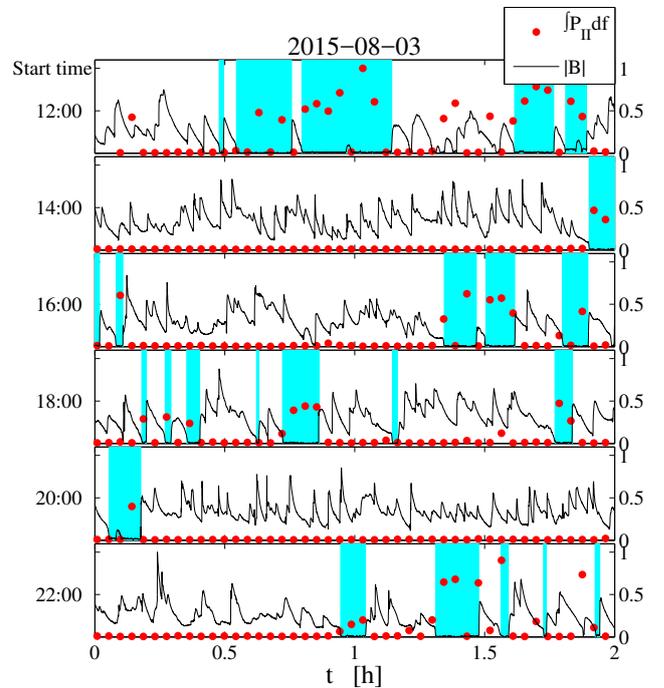

Figure 4. The power spectral density integrated over the interval $200\,\mathrm{Hz} < f < 1500\,\mathrm{Hz}$ (red dots) and the magnitude of the magnetic flux density *B* (black line). Both quantities have been normalised to the highest value observed during the twelve hour period. Each panel shows two hours of observations. The light blue areas mark the cavities identified by Goetz et al. (2016a).

observed outside these regions. First, the waves exist not only inside the cavity proper, but also at the boundary. In the example of the peak in wave power at 12:08 (first panel of Fig. 4), a decrease in B was observed just before the wave spectrum was recorded, indicating that the spacecraft was in the boundary region but did not pass completely through it into the cavity itself. Another example is the black curve in Fig. 3, which was recorded at the boundary and shows a power spectral density between those obtained completely inside and completely outside the boundary. Secondly, short cavity traversals may comprise too few magnetic field data points to allow identification. Since the time between wave observations is 160 s it may also happen that a complete cavity sighting happens when no wave measurement is performed.

To conclude this section we note that during this day, the waves are observed in the diamagnetic cavity and at its boundary, but not elsewhere.

2.3   Ion populations

The RPC-ICA instrument (Nilsson et al. 2007) measures the differential particle flux of ions in 16 sectors. During the period shown in Fig. 2, and most of that shown in Fig. 1, the instrument was operated in a high temporal resolution mode, where no scanning out of the nominal viewing plane was performed, and the energy sweep was reduced to 8 energy channels covering a range from 15 eV to 56 eV. One such energy sweep was performed every 16 s. Ion distribution functions are derived from the RPC-ICA data in the way described by Gunell et al. (2017). An offset to the energy scale was found when measurements first were performed at the comet (Nilsson et al. 2015a). In this work, we use an energy table that has been corrected accordingly (Nilsson et al. 2017; Stenberg Wieser et al. 2017). The spacecraft potential is determined by finding the value which puts the lowest energy ions at zero velocity. For 3 August 2015 the spacecraft potential value found in this way is −16.3 V. However, in the high temporal resolution mode, the energy sweep doesn't cover the lowest energies. This means that the spacecraft potential in reality may be a few volts less negative, in the vicinity of −13 V, which would be in better agreement with the Langmuir probe measurements presented in Sect. 2.4. Furthermore, it is seen in Fig. 2d that the energy of the ions increases during a few short periods, most noticeably at 18:51 when the spacecraft exited the diamagnetic cavity. This change in observed energy likely corresponds to a change in spacecraft potential, which is not precisely known.

The three distributions shown in Fig. 5 are all computed under the assumption of a −16.3 V spacecraft potential, although the actual potential may have varied between the distributions and could be a few volts less negative. Fig. 5 shows the ion distributions before the spacecraft entered the cavity (top panel), while it was inside it (middle panel), and after it left the cavity (bottom panel). The distribution has been rotated azimuthally to put the highest energy ions on the positive v_χ axis. All three distributions shown have been rotated by the same angle. The low distribution function values in the upper ($v_\zeta > 0$) part of all three panels correspond to sectors 10–13 that are blocked partially by the spacecraft body. The zero-flux segment diagonally down to the right
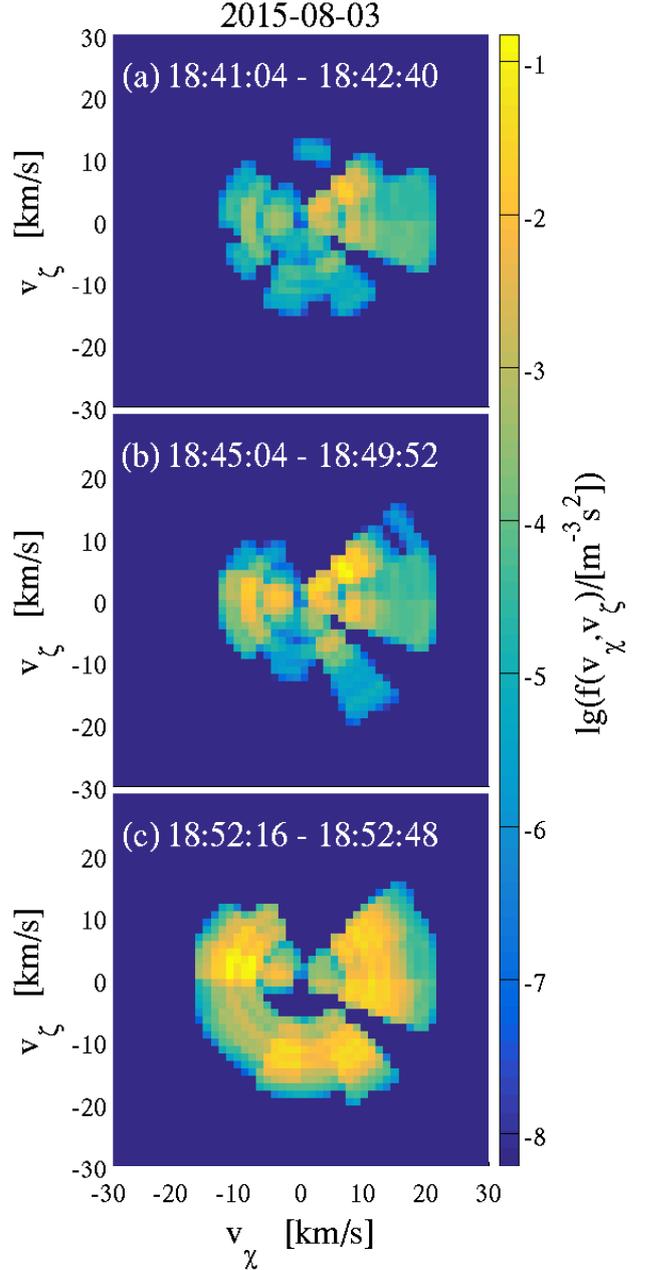

Figure 5. Two-dimensional water ion distribution functions. **(a)** Average of the six distributions recorded between 18:41:04 and 18:42:40 on 3 August 2015, that is, before the spacecraft entered the cavity. **(b)** Average of 18 distributions recorded inside the cavity between 18:45 and 18:50. **(c)** Average of two distributions recorded soon after the spacecraft left the cavity, between 18:52:16 and 18:52:48 on 3 August 2015.

($v_\chi > 0$, $v_\zeta < 0$) corresponds to sector 1, which has a particularly low sensitivity.

The shape of the distribution function is the same in the three cases. The distribution in Fig. 5c, recorded after the spacecraft left the cavity, but while it still was in the boundary region, is somewhat broader in velocity space. While such a broadening may indicate a higher ion temperature, it is more likely a result of a decreased spacecraft
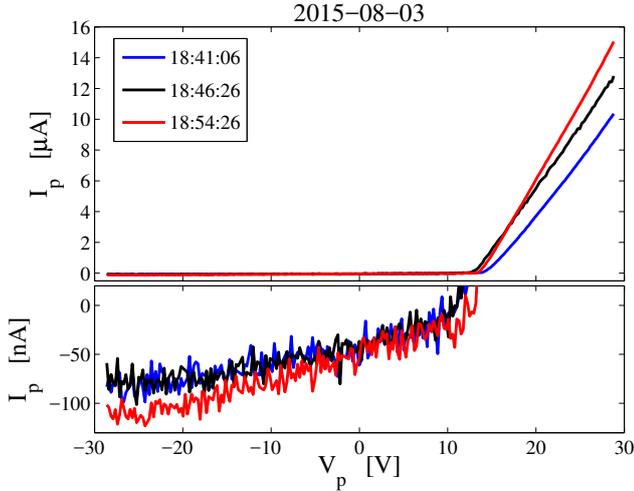
Figure 6. Langmuir probe current–voltage characteristics recorded by RPC-LAP probe 1 before the spacecraft entered the diamagnetic cavity (18:41, blue curve), while the spacecraft was in the cavity (18:46, black curve), and after the spacecraft had left the cavity (18:54, red curve). The upper panel shows the complete characteristic. In the lower panel, a different vertical scale is used in order to visualise the ion current.

potential as discussed above. The hole in the distribution in Fig. 5c for $-6\,\mathrm{km\,s^{-1}} \lesssim v_\zeta \lesssim 0$ indicates an asymmetry in the sheath surrounding the negatively charged spacecraft caused by an electric field present in the boundary region of the diamagnetic cavity.

To estimate the ion density from the RPC-ICA measurements, assumptions must be made for the regions of velocity space that are outside the field of view. Assuming that the distributions are isotropic, we arrive at densities in the range 10^7–$10^8\,\mathrm{m^{-3}}$ for the distribution shown in Fig. 5. This is 1–2 orders of magnitude lower than the plasma density observed by RPC-MIP shown in Fig. 2c. To maintain quasi-neutrality the vast majority of all ions must be hidden in the low energy range that we do not observe when RPC-ICA is in the high temporal resolution mode with its reduced energy range.

The ion distributions are similar in the diamagnetic cavity and outside it. The dominating component is a cold distribution that we cannot measure directly. Ions are formed by ionisation of the neutrals that emerge from the nucleus, and they will be cold in the absence of a heating process.

2.4 Probe measurements of electron and ion populations

The upper panel of Fig. 6 shows Langmuir probe current–voltage characteristics obtained by RPC-LAP probe 1, before, during, and after the cavity passage. The curves are similar to the one taken on 30 July 2015 that was analysed by Eriksson et al. (2017): the general shape of the curve is the same, the knee at which the sharp increase in current starts is at approximately the same probe potential, and the slope of the curve in the electron collecting regime is approximately the same. Following Eriksson et al. (2017) we make the interpretation that there is one cold ($k_B T_e \lesssim 0.1\,\mathrm{eV}$) and

one warm ($5\,\mathrm{eV} \lesssim k_B T_e \lesssim 10\,\mathrm{eV}$) electron population, and the spacecraft potential at the position of the probe, determined from the knee in the characteristic, is in the range $-14\,\mathrm{V} \lesssim V_{sc} \lesssim -12\,\mathrm{V}$. The cold distribution is responsible for the steep slope of the characteristic, and the warm distribution charges the spacecraft negatively. The determination of how the density is distributed between the two populations, and of what the exact values of their temperatures are, is fraught with uncertainty. In Sect. 3 we examine how different assumptions about the particle populations affect the ion acoustic waves.

The lower panel of Fig. 6 shows the ion current part of the probe characteristics. The slope of the black and blue curves, which were recorded inside the cavity, is about $2 \times 10^{-9}\,\mathrm{AV^{-1}}$. For H_2O^+ ions at $n = 10^9\,\mathrm{m^{-3}}$ and a probe radius of 2.5 cm, this is consistent with a cold, $T_i = 0$, ion population with a bulk velocity of $1.7\,\mathrm{km\,s^{-1}}$ (Mott-Smith & Langmuir 1926). Vigren & Eriksson (2017) obtained similar drift speeds in a 1D model of the ambipolar electric field.

3 WAVE THEORY

Since both the ion and electron distributions are known only approximately, we compute dispersion relations for five different assumed distributions to see what the consequences are for the generation of waves in the diamagnetic cavity. The computational method is based on simple pole expansions of the distribution functions (Löfgren & Gunell 1997; Tjulin et al. 2000; Gunell & Skiff 2001, 2002; Tjulin & André 2002). It was reviewed by Gunell et al. (2017) in the context of waves at comets, also including computer programs to perform the calculation. Here, we only describe the distribution functions used in this work.

For the purpose of wave theory, the plasma is assumed to be unmagnetised. This is reasonable because the magnetic field is at most 1 nT, which means the electron cyclotron frequency is below 28 Hz, which in turn is below the range of the observed waves. The gyro radii for a 0.1 eV electron and a 0.01 eV H_2O^+ ion are more than 1 km and 61 km, respectively. That is much greater than the wavelength of ion acoustic waves, which the following calculations show is of the order of 1–10 m.

In each of the five cases shown in Table 1 we include three populations: H_2O^+ ions, cold electrons, and warm electrons. Each population is described by an approximate drifting Maxwellian

$$M(v) = \left[1 + \frac{(v - v_d)^2}{2v_t^2} + \ldots + \frac{1}{m!}\left(\frac{(v - v_d)^2}{2v_t^2}\right)^m \right]^{-1}, \quad (1)$$

where M is the reciprocal of a Taylor expansion of

$\exp\left((v - v_d)^2 / \left(2v_t^2\right) \right)$,

v_d is the average drift velocity, v_t is the thermal speed, and m is the number of terms included in the expansion. Here, we have used $m = 5$ for each of the two electron populations, and $m = 6$ for the ion population. We compute the dispersion relations in the ion rest frame, $v_{di} = 0$. Assuming quasi-neutrality the ion density is $n_i = n_{ec} + n_{ew}$, where n_{ec} and n_{ew} are the densities of the cold and warm electron populations, respectively. The other parameters are shown in Table 1. In a plasma composed of different populations, α, these are

Table 1. Parameters of the electron and H_2O^+ distributions for which dispersion relations are calculated and shown in Fig. 7. T_i, T_{ec}, and T_{ew} are the temperatures of the ions, the cold electrons, and the warm electrons, respectively; the densities of the cold and warm electrons are n_{ec} and n_{ew} respectively; and the corresponding drift velocities are v_{dec} and v_{dew}. In the last column D means that the ion acoustic mode is damped and G that it is growing.

#	ions $k_B T_i$ [eV]	cold electrons $k_B T_{ec}$ [eV]	v_{dec} [km s^{-1}]	n_{ec} [m^{-3}]	warm electrons $k_B T_{ew}$ [eV]	v_{dew} [km s^{-1}]	n_{ew} [m^{-3}]	J [nA m^{-2}]	
1	0.02	0.1	0	5×10^8	10	0	5×10^8	0	D
2	0.02	0.1	8.7	5×10^8	10	0	5×10^8	697	G
3	0.01	0.1	2.0	5×10^8	10	0	5×10^8	160	G
4	0.01	0.1	1.6	2×10^8	10	0	8×10^8	51	G
5	0.02	0.1	8.7	5×10^8	10	-8.7	5×10^8	0	G

weighted by their respective plasma frequency squared to form the dielectric function (e.g. Krall & Trivelpiece 1973)

$$\epsilon(k, \omega) = 1 + \sum_\alpha \frac{\omega_{p\alpha}^2}{k^2} \int \frac{k \, df_\alpha(u)/du}{\omega - ku} \, du. \tag{2}$$

For the normal modes, we assume a real value for the wave number k and a complex angular frequency ω, which satisfies

$$\epsilon(k, \omega) = 0. \tag{3}$$

Distribution 1 in Table 1 is our nominal case, where none of the populations are drifting. The cold and warm electrons have equal densities. The dispersion relation is shown by the black curves in Fig. 7. The upper panels show the dispersion relations, given by the real part of ω as a function of k, and the lower panels the damping rates γ. The right-hand panels show a zoomed-in view of the long wavelength range $0 \leq k \leq 5 \, \mathrm{m}^{-1}$. Only the ion acoustic modes are shown. Having two electron temperatures, these distributions can also support electron acoustic waves. However, since those would only be observable in a much higher frequency range than what we can measure, we do not show their dispersion relations. The black curves shows that there are ion acoustic waves in the frequency range of the observations, but it also shows that the damping is significant. Ion acoustic waves are heavily damped unless $T_e \gg T_i$. Here we have chosen $k_B T_i = 0.02 \, \mathrm{eV}$, and a cold electron component with temperature, $k_B T_e = 0.1 \, \mathrm{eV}$, that is only five times higher.

Differing ion and electron drift velocities can be caused by an ambipolar electric field, as modelled by Vigren & Eriksson (2017), or by acceleration by an electric field arising in connection with the bulges on the boundary that are discussed in Sect. 4. The relative drift velocities used below are chosen in order to illustrate what is required to drive the distribution unstable in the different cases. We have not tried to find the exact value of velocity that is on the border between stable and unstable distributions. By assigning a drift velocity of $v_{dec} = 8.7 \, \mathrm{km \, s^{-1}}$ to the cold electrons we obtain distribution 2, shown by the dashed green curves in Fig. 7. The damping rate then becomes negative, which means the wave is growing, for $k \lesssim 1 \, \mathrm{m}^{-1}$. The electrons are moving in the frame of the ions, and this corresponds to a current density of $0.7 \, \mu \mathrm{A \, m^{-2}}$ as shown in Table 1. Current-driven ion cyclotron waves have been observed in laboratory experiments (Sato et al. 1976; Michelsen et al. 1979), and the parameter

regimes where these waves grow were mapped out theoretically by Stringer (1964). The magnetic field measurements show that $B < 1 \, \mathrm{nT}$. While the magnetic field depends on the current, wave growth depends on the current density. Thus, current-driven waves can be consistent with the magnetic field observations, if the spatial extent of the current channel is small enough. This is discussed further at the end of this section.

In distribution 3, the ion temperature has been lowered to $k_B T_i = 0.01 \, \mathrm{eV}$. That increases the electron to ion temperature ratio, and therefore the waves can be made unstable at a lower electron drift speed. The result is shown by the red curves in Fig. 7, where red curve in the lower right panel is below zero for $0 < k < 0.6 \, \mathrm{m}^{-1}$. Distribution 4 contains 20% cold and 80% warm electrons, instead of the equal numbers of warm and cold electrons in the other distributions. Distribution 4 is unstable at an even lower drift speed than distribution 3 and at a significantly lower current density. However, the maximum growth rate occurs at $k \approx 3.8 \, \mathrm{m}^{-1}$, as seen by the blue curve in the lower right panel of Fig. 7. The upper right panel shows that this corresponds to a frequency of approximately 860 Hz. Hence, the agreement with observations is worse for distribution 4 than for the other distributions, as all the spectra shown in Fig. 3 peak at significantly lower frequencies.

Finally, distribution 5 has all the same temperatures and densities as distribution 2; the cold electrons also have the same drift velocity. The difference is that the warm electrons have been given a drift velocity $v_{dew} = -8.7 \, \mathrm{km \, s^{-1}}$, counteracting the cold electron drift so that the net current is zero. The dispersion relation is so similar to that of distribution 2 that the curves cannot be distinguished on the scales of any of the panels in Fig. 7, and therefore both cases are shown by the dashed green curves. This example shows that it is the drift of the cold population that is important for dispersion relations and wave growth. This is a result of the large difference in thermal speeds between the two electron distribution, which renders a fixed drift speed more influential on the slope of the total distribution function when it is applied to the cold than to the warm electron population. It is not likely that such an unstable zero-current distribution would appear naturally at the comet, as that would require a mechanism that accelerates the two electron populations in opposite direction to exactly the same speed.

The distribution functions of electrons and ions are not known precisely. From these examples of dispersion rela-
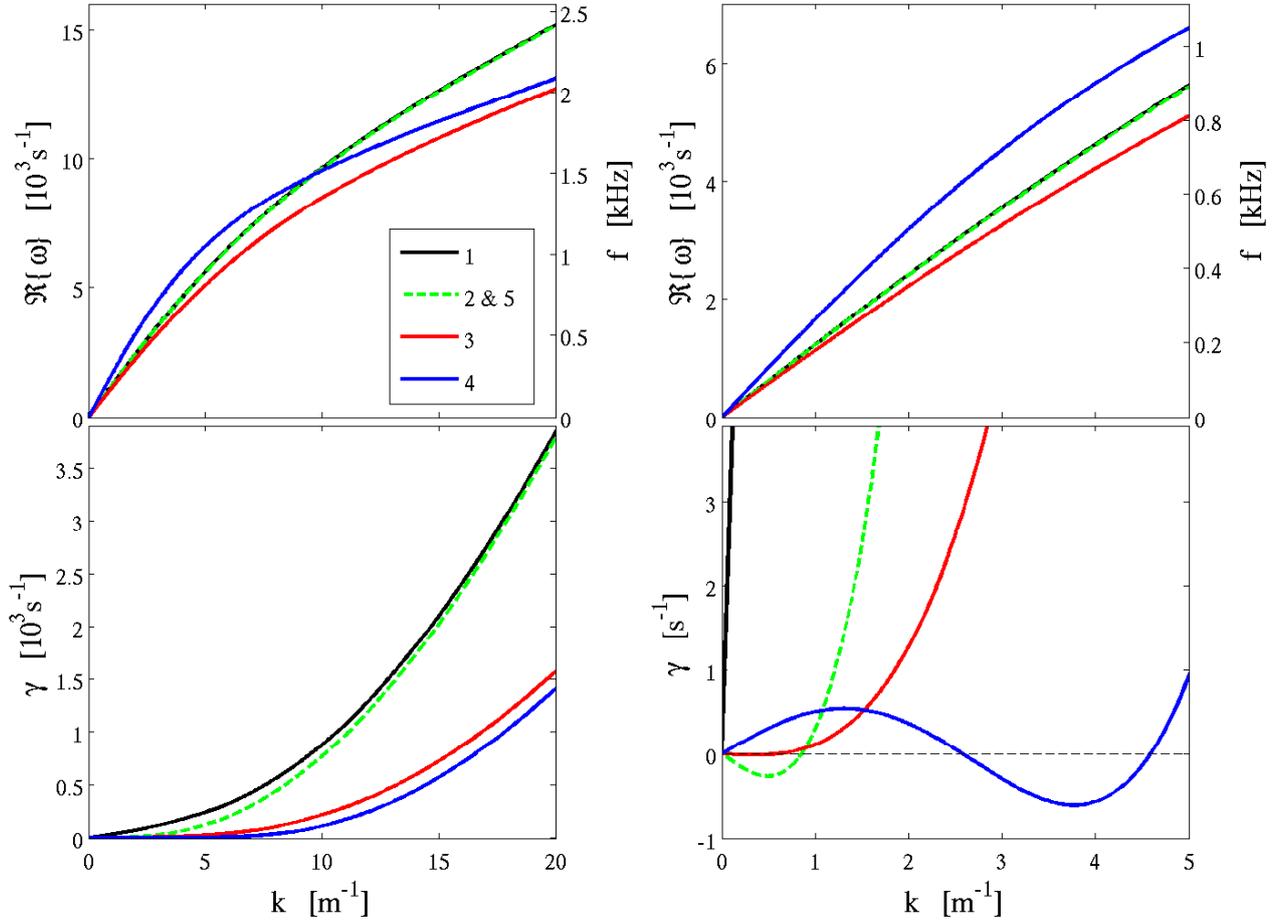
Figure 7. Dispersion relations (upper panels) and damping rates (lower panels) of ion acoustic waves computed for the distributions detailed in Table 1. The right-hand panels show a zoomed-in view of the long-wavelength range $0 \leq k \leq 5\,\mathrm{m}^{-1}$. The results for distributions 2 and 5, being indistinguishably close, are shown by the same curve.

tions, we can draw the conclusion that the observed wave spectrum is consistent with ion acoustic waves in a plasma with two electron populations of different temperatures, where the cold population has a drift velocity with respect to the ions. The peak in the growth rate for the red and green curves in Fig. 7 is near $k = 0.5\,\mathrm{m}^{-1}$, which corresponds to a wavelength of $\lambda \approx 13\,\mathrm{m}$. For comparison, the Debye lengths of the cold and warm electron populations are $0.1\,\mathrm{m}$ and $1\,\mathrm{m}$ respectively. The wave spectrum falls off with increasing frequency as shown in Fig. 3, and with the dispersion relations of Fig. 7, $\lambda \approx 0.6\,\mathrm{m}$ at $1.5\,\mathrm{kHz}$.

The unstable distributions in Table 1 all carry a current, except distribution 5 which is a hypothetical example. The observations by Goetz et al. (2016a) confined the magnetic field to $B < 1\,\mathrm{nT}$. The variation of the field inside the cavity is shown in more detail in Fig. 8 for the cavity observation between 18:43:20 and 18:51:43, which we use as an example in this paper. From Fig. 8 we conclude that $1\,\mathrm{nT}$ is a reasonable value of the maximum observed B. We can estimate the maximum size a current channel could have without generating higher magnetic fields than that. On the surface of a current-carrying slab of thickness d, the magnetic field is $B = 0.5\mu_0 J d$, which means that for the J values 697, 160,
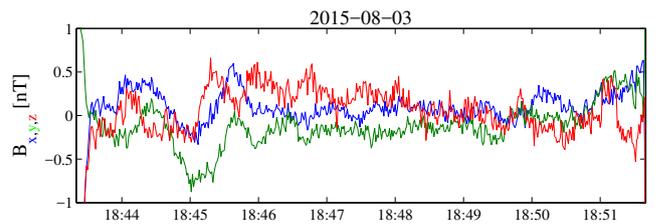

Figure 8. The three components of the magnetic flux density **B** seen by RPC-MAG for the cavity passage shown in Fig. 2.

and $51\,\mathrm{nA\,m}^{-2}$ in Table 1, the thicknesses $d = 2.3$, 9.9, and $31\,\mathrm{km}$, respectively yield a field of $1\,\mathrm{nT}$.

4 CONCLUSIONS AND DISCUSSION

We have observed wave spectra using the Langmuir probe instrument onboard the Rosetta spacecraft, when it was in the diamagnetic cavity of comet 67P/Churyumov-Gerasimenko. The wave spectrum peaks near $200\,\mathrm{Hz}$. It falls off for higher frequencies, reaching the noise floor at approximately $1.5\,\mathrm{kHz}$. The waves are seen only when the spacecraft is in

the cavity or at its boundary. When the spacecraft is in the plasma outside the cavity, no waves are seen. We interpret these waves as ion acoustic waves in the water ion plasma of the comet. What generates these waves? We propose that they are driven by a current flowing through the plasma in the part of the diamagnetic cavity near the boundary, and that the spacecraft never went deep enough into the cavity to reach beyond this region. However, there are a few other possibilities that deserve a brief discussion.

The generation mechanism is unlikely to be an ion–ion instability, as we observe no sign of an ion beam in the data. There does remain a possibility that such a beam escapes detection, since the sensitivity of the ion instrument is low at low energies, and since, in the high temporal resolution mode used here, we have only two-dimensional ion measurements in one plane and an energy sweep that does not cover the lowest energies. If an ion beam exists, it would have to be generated in the same cold plasma that is dominating in the diamagnetic cavity, since a warmer beam, or one that has been dispersed due to a distributed source region, would have a detectable ion tail.

An instability created by an anisotropic ion distribution cannot be ruled out completely, since the bulk of the ion distribution is at energies too low for us to observe directly. However, we find it unlikely that an anisotropy could be maintained in the unmagnetised plasma of the diamagnetic cavity. The anisotropy in Fig. 5c, which we interpret as an indication of an anisotropic sheath around the spacecraft rather than an anisotropic ion distribution in the surrounding plasma, was measured outside the cavity and thus outside the region where ion acoustic waves are observed.

Another possibility is that the waves are indeed current-driven, but only in the boundary layer itself, and that they propagate from the boundary into the cavity, but not away in the outside plasma. This hypothesis would require that the damping in the cavity to be significantly smaller than that on the outside of the boundary. It is possible that a heating mechanism could be active outside the boundary, leading to a warmer ion distribution there and hence to stronger damping. However, already distribution 1 in Table 1 at $k_BT_i = 0.02\,\mathrm{eV}$ shows significant damping, and in the absence of an electron drift one would expect considerable damping also in the cavity. Also, for this idea to hold one would expect a decrease in wave power as the spacecraft moves away from the boundary farther into the cavity. There are a few isolated points of low power in the cavity in Fig. 4, but there is no systematic behaviour that could confirm the hypothesis. We deem it more likely that the source region of the wave extends to all the parts of the diamagnetic cavity that have been visited by Rosetta.

What could cause a spatially limited current channel consistent with these observations? The estimates in Sect. 3 puts its thickness in a range from a few kilometres to a few tens of kilometres. The spacecraft was approximately 220 km from the nucleus when these observations were made. Thus, our estimates correspond to a thickness that is $1\,\% - 14\,\%$ of the cavity radius. The values are approximate, but large scale current closure through the centre of the cavity can be ruled out, as it would generate too strong a magnetic field. We can also dismiss the possibility that the current is confined to the outer regions of the cavity due to collisional resistivity in the interior. Using the neutral density

of $4 \times 10^{13}\,\mathrm{m}^{-3}$, measured by the ROSINA-COPS instrument (Balsiger et al. 2007), and extrapolating inward using a Haser model, we estimate the resistivity to be insignificant everywhere except within 10–20 km from the nucleus.

Goetz et al. (2016a) performed a minimum variance analysis of the magnetic field at the cavity crossings and found the boundary normal direction to be consistent with elliptically shaped bulges on the boundary. Similarly, Henri et al. (2017) suggest that the parts of the boundary bend outward due to a Rayleigh-Taylor-like instability. If the boundary is pushed outward, forming a bulge, the magnetic field at the tip of the bulge would be stronger than at the sides of it. This means that also the current in the boundary layer would have to be stronger at the peak of the protrusion, and some of that current could close through the bulging cavity. The spacecraft is not moving significantly in relation to the nucleus of the comet. It is therefore reasonable to assume that all the diamagnetic cavity observations presented here happened due to extrusions moving over an effectively stationary spacecraft. We propose that all our observations took place in bulges, and that currents are running through these protuberant parts, generating current-driven ion acoustic waves. The nature of the wave environment deeper inside the diamagnetic cavity will have to be determined by future space missions.

REFERENCES

Balsiger H., et al., 2007, Space Science Reviews, 128, 745
Behar E., Nilsson H., Stenberg Wieser G., Nemeth Z., Broiles T. W., Richter I., 2016a, Geophys. Res. Lett., 43, 1411
Behar E., Lindkvist J., Nilsson H., Holmström M., Stenberg Wieser G., Ramstad R., Götz C., 2016b, Astronomy & Astrophysics, 596, A42
Cravens T. E., 1987, Advances in Space Research, 7, 147
Eriksson A. I., et al., 2007, Space Science Reviews, 128, 729
Eriksson A. I., et al., 2017, Astronomy & Astrophysics, in press
Glassmeier K.-H., 2017, Philosophical Transactions of the Royal Society A.
Glassmeier K.-H., Boehnhardt H., Koschny D., Kührt E., Richter I., 2007a, Space Science Reviews, 128, 1
Glassmeier K.-H., et al., 2007b, Space Science Reviews, 128, 649
Goetz C., et al., 2016a, Monthly Notices of the Royal Astronomical Society, 462, S459
Goetz C., et al., 2016b, Astronomy & Astrophysics, 588, A24
Gunell H., Skiff F., 2001, Physics of Plasmas, 8, 3550
Gunell H., Skiff F., 2002, Physics of Plasmas, 9, 2585
Gunell H., et al., 2015, Planetary and Space Science, 119, 13

Gunell H., et al., 2017, Astronomy and Astrophysics, 600, A3

Gurnett D. A., et al., 1985, Geophys. Res. Lett., 12, 851

Haerendel G., 1987, Geophys. Res. Lett., 14, 673

Haerendel G., Paschmann G., Baumjohann W., Carlson C. W., 1986, Nature, 320, 720

Henri P., et al., 2017, Monthly Notices of the Royal Astronomical Society, this volume, submitted

Karlsson T., et al., 2017, Geophys. Res. Lett., 44, 1641

Koenders C., Glassmeier K.-H., Richter I., Ranocha H., Motschmann U., 2015, Planetary and Space Science, 105, 101

Krall N. A., Trivelpiece A. W., 1973, Principles of Plasma Physics. McGraw-Hill, New York

Löfgren T., Gunell H., 1997, Physics of Plasmas, 4, 3469

Mandt K. E., et al., 2016, Monthly Notices of the Royal Astronomical Society

Michelsen P., Pecseli H. L., Juul Rasmussen J., Schrittwieser R., 1979, Plasma Physics, 21, 61

Mott-Smith H. M., Langmuir I., 1926, Physical Review, 28, 727

Nemeth Z., et al., 2016, Monthly Notices of the Royal Astronomical Society, 462, S415

Neubauer F. M., et al., 1986, Nature, 321, 352

Nilsson H., et al., 2007, Space Science Reviews, 128, 671

Nilsson H., et al., 2015a, Science, 347

Nilsson H., et al., 2015b, Astronomy & Astrophysics, 583, A20

Nilsson H., et al., 2017, Monthly Notices of the Royal Astronomical Society, this volume, submitted

Odelstad E., et al., 2015, Geophys. Res. Lett., 42, 10

Oya H., Morioka A., Miyake W., Smith E. J., Tsurutani B. T., 1986, Nature, 321, 307

Richter I., et al., 2015, Annales Geophysicae, pp 1031–1036

Richter I., et al., 2016, Annales Geophysicae, 34, 609

Rubin M., Gombosi T. I., Hansen K. C., Ip W.-H., Kartalev M. D., Koenders C., Tóth G., 2015, Earth, Moon, and Planets, 116, 141

Sato N., Popa G., Märk E., Mravlag E., Schrittwieser R., 1976, Physics of Fluids, 19, 70

Scarf F. L., Ferdinand V., Coroniti V., Kennel C. F., Gurnett D. A., Ip W.-H., Smith E. J., 1986, Science, 232, 377

Simon Wedlund C., et al., 2016, Astronomy & Astrophysics, 587, A154

Simon Wedlund C., et al., 2017, Astronomy & Astrophysics, in press

Stenberg Wieser G., et al., 2017, Monthly Notices of the Royal Astronomical Society, this volume, submitted

Stringer T. E., 1964, Journal of Nuclear Energy, 6, 267

Tjulin A., André M., 2002, Physics of Plasmas, 9, 1775

Tjulin A., Eriksson A. I., André M., 2000, Journal of Plasma Physics, 64, 287

Trotignon J. G., et al., 2007, Space Science Reviews, 128, 713

Vigren E., Eriksson A. I., 2017, The Astronomical Journal, 153, 150

Vigren E., Galand M., 2013, Astrophysical Journal, 772, 33

This paper has been typeset from a TEX/LATEX file prepared by the author.